Plasmonic Mach-Zehnder interferometer based on graphene sheets and resonators

JICHENG WANG[a,b,*], XIUYE LIANG[a], XIUSHAN XIA[a], BAOJIE TANG[a]
[a]*School of Science, Jiangnan University, Wuxi 214122, China*
[b]*Key Laboratory of Semiconductor Materials Science, Institute of Semiconductors, Chinese Academy of Sciences, 912, Beijing 100083, P.R. China*

We theoretically design the plasmonic structures based on the coupling between the graphene sheets and resonators for the mid-IR region, which can be used to construct the ultra-compact fast-tunable optical filter, splitter, 1×2 digital optical switch, or Mach-Zehnder interferometer. Electrical tunability of the system by tiny change of the Fermi level (chemical potential) of the graphene is realized. In addition, the quality and sensitivity of the system can be optimized by changing the coupling distance. The finite element method results are verified by the resonance theory of the rings.

(Received December 14, 2015; accepted February 10, 2017)

Keywords: Graphene plamonics, Mach-Zehnder interferometer, Resonator, Fermi lovel

1. Introduction

Surface plasmon polaritons (SPPs), coupled modes of plasmons and photons, are confined to the metal-dielectric interface [1]. When the SPPs propagate along flat interfaces, the electromagnetic field is tightly confined at the interface and decays exponentially into the two adjoining media. Owing to their remarkable ability to break the diffraction limit and manipulate light at subwavelength scales, SPPs in noble metals have promising many applications on the devices in highly integrated optical circuits [2, 3]. Numerous devices based on SPPs such as filters [4, 5], splitters [6], couplers [7], Y-shaped combiners [8], and Mach-Zehnder interferometers [9], have been investigated theoretically and demonstrated experimentally. However, the performance of traditional noble metals based plasmonics are hampered because of the difficulty in varying and controlling their permittivity functions. In these cases, the ability to actively tune plasmon devices remains a challenge.

A monolayer graphene [10], with remarkable optical properties, such as extreme confinement, dynamic tunability [11, 12], and low losses [13], has been vigorously researched as a promising platform for plasmonics during recent years [14-18]. Particularly, the surface conductivity of graphene could be dynamically tuned by electrochemical potential via gate voltage, electric field, magnetic field, and chemical doping [19]. This increasingly promotes the development of active plasmonic devices including absorbers [20], polarizers [21], transformation optical devices [22], optical modulators [23-25], sensors [26], filters [27, 28] and graphene waveguide [29, 30]. Nikitin *et al*. have discussed the edge and waveguide terahertz surface plasmon modes in graphene microrib bons and found that the edge modes may enhance the EM coupling between objects [31]. *Huanget al*. have proposed to use monolayer graphene as a plasmonic waveguide to construct a graphene ring resonator [32]. Thus, monolayer graphene, which has exciting optoelectronic transport properties suitable for actively tunable optoelectronic devices, is a building block for tunable sensors, couplers, filters, switchers, and interferometers.

In this letter, we theoretically design the plasmonic structures based on the coupling between the graphene sheets and ring resonators for the mid-IR region, which can be used to construct the ultra-compact fast-tunable optical filter, splitter, 1×2 digital optical switch, or Mach-Zehnder interferometer. The coupling between the graphene sheets and graphene ring resonators has been thoroughly studied. By changing the Fermi level (chemical potential) in the graphene rings, the resonant wavelengths can be tuned expediently. The influences of the coupling distance on the quality and the sensitivity of the system also have been discussed. These actively tunable and electrically controlled structures are qualitatively different from traditional surface plasmon polaritons (SPPs) ones which are based on noble metals. Those finite element method (FEM) results are verified by the resonance theory of the rings.

2. Basic single channel graphene coupling system

As shown schematically in Fig. 1, the basic graphene plasmonic coupling system consists of two graphene sheets coupled by a graphene ring. The graphene ring is in fact curved monolayer graphene that is rolled into a cylindrical shape. For simplicity on simulation, the graphene-based system is assumed to be suspended in air, while the mediums can be SiO_2 in the actual manufacturing. The planar graphene sheet plays the role of the waveguide and the antisymmetric SPP mode of the monolayer graphene injected from the left port will travel in the ring and out of the right port. The optical conductivity of graphene is governed by the Kubo formalism including the interband and intraband transition contributions [33]. The surface conductivity of graphene σ_g, is governed by the Kubo formula:

$$\sigma_g = \frac{ie^2E_f/\pi\hbar^2}{\omega+i\tau^{-1}} + \frac{ie^2}{4\pi\hbar}\ln\left[\frac{2E_f-(\omega+i\tau^{-1})\hbar}{2E_f+(\omega+i\tau^{-1})\hbar}\right] + \frac{ie^2k_BT}{\pi\hbar^2(\omega+i\tau^{-1})}\ln\left[\exp\left(-\frac{E_f}{k_BT}\right)+1\right], \quad (1)$$

It depends on temperature T, Fermi level E_f, momentum relaxation time τ, and photon frequency. In our analysis, the employed incident light is in the mid-infrared range where the intraband transition contribution dominates in monolayer graphene [34]. Under this condition, the optical conductivity is simplified to

$$\sigma_g(\omega) = \frac{ie^2E_f/\pi\hbar^2}{\omega+i\tau^{-1}}, \quad (2)$$

where$e$ is the electron charge, E_f represents the absolute value of the Fermi level and the carrier relaxation time $\tau = \mu E_f/(ev_f^2)$ relates to the carrier mobility μ and Fermi velocity $v_f = 10^6$ m/s in graphene. The equivalent permittivity of graphene is given by the equation [22]: $\varepsilon_{g,eq} = 1 + i\sigma_g\eta_0/(k_0\Delta)$, where $\eta_0 \approx 377\Omega$ is the intrinsic impedance of air and $k_0 = 2\pi/\lambda$ is wavenumber in vacuum.

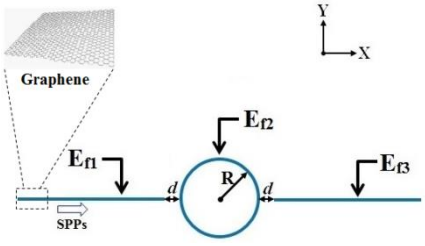

Fig. 1. Side view of the basic single channel graphene coupling system: R is the radius of the graphene ring; d is the coupling distance between the graphene sheets and graphene ring; E_{f1}, E_{f3}, and E_{f2} represent the gate voltages on two graphene sheets and the graphene ring, respectively

In our simulations, the thickness of monolayer graphene and graphene ring are modeled as Δ=0.5nm, and the carrier mobility is reasonably chosen to be μ= 20000 cm^2 V^{-1} s^{-1} from experiment results [10,20]. The TM-polarized surface plasmon polaritons (SPPs) supported by single-layer graphene is only in consideration for the investigation. The dispersion relation of this TM SPPs surface wave follows the equation:

$$\beta_{spp} = k_0\sqrt{1-(\frac{2}{\eta_0\sigma_g})^2}, \quad (3)$$

where β_{spp} is the propagation constant of graphene SPPs. Another important parameter derived from the above equation is the effective refractive index of graphene SPPs$N_{spp}=\beta_{spp}/k_0$, which shows the ability to confine SPPs on graphene. The propagation length is defined as L_{spp}=1/Im(β_{spp}) featuring the SPP spropagation loss in graphene. Furthermore, it should be noted that the dispersion relation of SPPs on monolayer graphene works on graphene rings as well [35]. The dependences of Re(N_{spp}) and L_{spp} on the Fermi level E_f and incident light wavelength λ are shown in Fig. 2. Obviously, from Fig. 2(a), Re(N_{spp}) increases as the Fermi level E_f decreases for a fixed wavelength, which means that SPPs are better confined at a lower Fermi level. Nevertheless, the tendency in Fig. 2(b) is evidently opposite to that in Fig. 2(a) indicating that a lower Fermi level gives a shorter propagation length. Thus, both these important factors should be taken into consideration in the design of PIT systems. Interestingly, Re(N_{spp})varies greatly when the Fermi level is changed slightly, which provides a way to actively control our configuration.

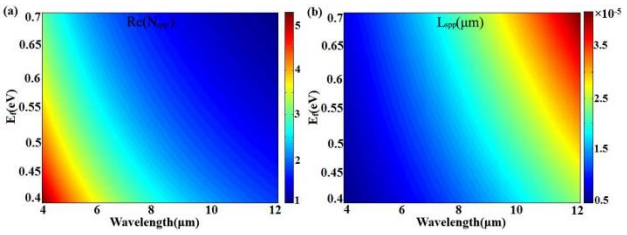

Fig. 2. (a) Real part of effective refractive index for graphene SPPs as a function of incident wavelength and Fermi level. (b) Dependence of propagation length L_{spp} on incident wavelength and the Fermi level

At first, the influences of coupling distance d between the graphene waveguides and resonator ring on the resonant modes have been investigated via numerical simulation, as shown in Fig. 3. The Fermi level on graphene sheets and the graphene ring are fixed at 0.4 eV and 0.5 eV, respectively. The radius of the graphene ring is assumed to be 100 nm. The coupling distance d varies from 5nm to 50nm. The two-dimensional numerical simulations are carried out in the configurations using the FEM. As shown in Fig. 3(a), the transmission spectra show multiple pronounced transmittance peaks

corresponding to each resonant mode. The resonance wavelength of SPPs on graphene ring should follow the phase-matching equation [32]:

$$\mathrm{Re}(\beta_{spp}) \cdot 2\pi R = 2m\pi, \quad (4)$$

where m is a positive integer, resonance mode number. With the increasing of coupling distance d, the transmission peaks get smaller and a little red-shift can be observed. This is because the increment of d weakens the coupling between graphene waveguides and ring and adds more phase delay. As the coupling distance increases, the full width at half-maximum (FWHM) of the transmission spectra decreases, as shown in Fig. 3(b), which shows the dependence of the FWHM of second-order, third-order and fourth-order modes on the coupling distance. At the same time, the height difference (HD) of the transmission peak is changed correspondingly. Thus, the coupling distance affects the quality of the transmission peaks and the sensitivity of the system. In order to improve the sensitivity of the system, we need to obtain transmission peaks with a smaller FWHM and larger HD. But the transmission peak values will decrease correspondingly. Certainly, we can optimize the transmission spectrum to meet different needs by choosing proper coupling distance.

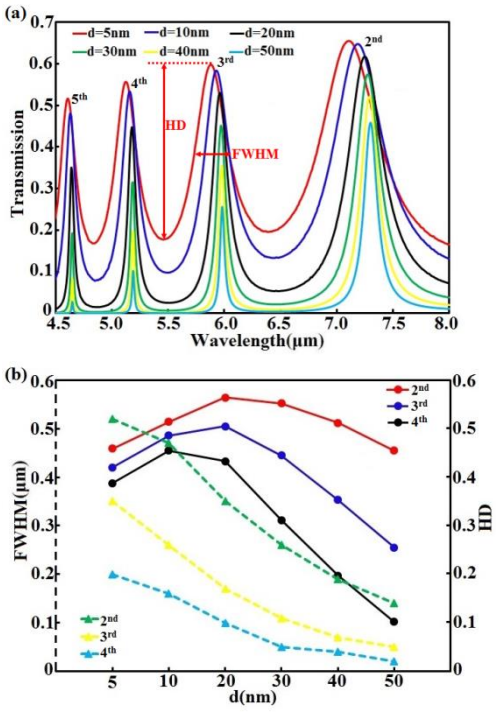

Fig. 3.(a) Transmission spectra of the basic single channel graphene coupling system with coupling distance d varying from 5 nm to 50 nm at same radius of the graphene ring (R=100 nm) and same Fermi levels (E_{f2} = 0.5 eV) on the graphene ring. (b) Dependence of FWHM and HD of the three order modes on coupling length d

Next, we investigated the influence of the graphene ring's Fermi level E_f on the resonance wavelengths. The radius of the graphene ring *R*and the coupling distance d are assumed to be 100 nm, 20 nm, respectively. The Fermi level on graphene sheets are fixed at 0.4 eV, while the Fermi level on graphene ring varies from 0.46 eV to 0.54 eV. Fig. 4(a) plots the transmission spectra for the proposed structure with various Fermi levels. The most intriguing phenomenon of this structure is that all the spectra blue shift at a large wavelength range with a slight increase of the Fermi level on the graphene ring. As shown in Fig. 4(b), the resonant modes of the simulation results agree well with the theoretical predictions determined from Eq. (4). It should be noted the phase delay from the coupling distance leads to the slight discrepancy which can be compromised by enlarging coupling distance or considering high-order resonant modes. Therefore, electrical tuning of this graphene based plasmonic filter can be achieved by adjusting the Fermi level of graphene.

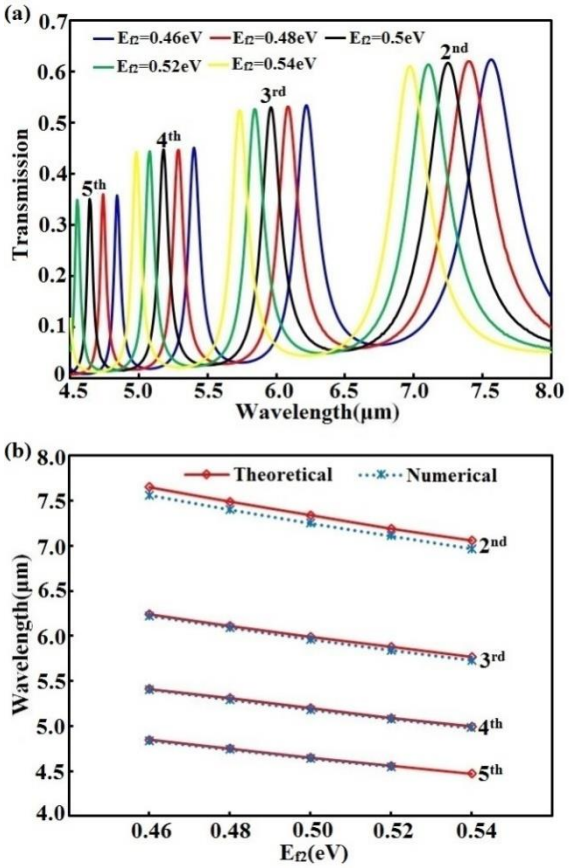

Fig. 4.(a) Transmission spectra for the graphene ring with different Fermi levels E_{f2}.(b) The dependence of the resonant wavelength of the simulation results (dashed line) and theoretical results (solid line, calculated from Eq. (4)) on the Fermi levels E_{f2} of the graphene ring

To explore the physics of the resonance, Fig. 5(a-e) visually illustrate the magnetic intensity distributions $|H_z|$ and normalized electric field distributions corresponding

to the transparency wavelengths 7.11 μm, 5.88 μm, 5.12 μm, 4.61 μm and 8.25 μm for second-order, third-order, fourth-order and fifth-order, non-resonant modes. The parameters d, R, E_{f1}, E_{f2} and E_{f3} are fixed at 5 nm, 100 nm, 0.4 eV, 0.5 eV and 0.4 eV, respectively. Apparently, the graphene SPPs will be only enhanced in the ring at resonance wavelengths and then efficiently coupled to the output graphene waveguide. For higher order resonant modes, less energy can be transported to the output due to the weak coupling between the graphene waveguides and ring since less graphene SPPs field extends off them. When the graphene ring is in non resonant, only little incident energies can successfully pass through the right waveguide. Supposing the gate voltage yields a Fermi level ofE_{f0} = 0.05 eV in the ring, the biased graphene ring will behave as dielectric and no longer support SPPs because the inter band transition of electrons occur at this Fermi level [22,32]. Fig. 5(f) shows the off-state when the Fermi level on graphene ring is 0.05 eV.

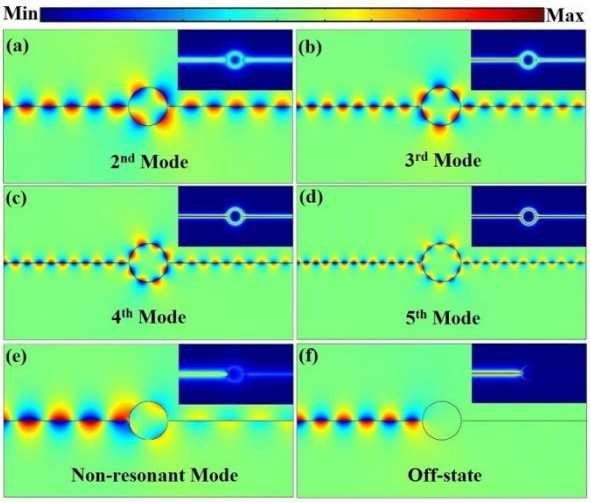

Fig. 5.(a-f) Magnetic intensity distributions $|H_z|$ corresponding to the transparency wavelengths 7.11 μm, 5.88 μm, 5.12 μm, 4.61 μm, 8.25 μm, and 7.11 μm for second-order mode, third-order mode, fourth-order mode, fifth-order mode, non-resonant mode, and off-state, respectively. The insets denote the corresponding normalized electric field distributions of graphene SPPs in the basic system

3. Dual channel graphene coupling system

To make full use of the efficient coupling between the graphene sheets and the ring, one more parallel channel is added to the basic structure as shown in Fig. 6. Thus, the input energy may have two feasible output waveguides. The spaces between the graphene ring and two output graphene sheets are both 50 nm. The radius of the graphene ring and the distance d between the input sheet and the graphene ring are fixed at 100 nm, 5 nm, respectively. Fig. 6(a) depicts the magnetic intensity distributions $|H_z|$ and normalized electric field distributions of SPPs in a 3 dB waveguide splitter when the resonance wavelength is 5.88 μm. Since the surface conductivity of graphene is tunable by gate voltage, the coupling process can be controlled. When one of the output graphene sheets in the splitter is biased, its Fermi level hence the surface conductivity should be accordingly modified. Supposing the gate voltage yields a Fermi level of E_{f0} = 0.05 eV in the lower graphene sheet, the SPPs from the input graphene sheet will be coupled only to the upper one which is not biased, see Fig. 6(b). In the same way, the incident energy can also be channeled to only the lower output graphene sheet, as is displayed in Fig. 6(c). Moreover, Fig. 6(d) shows the condition when both two output graphene sheets are biased. Until now, an effective digital optical switch has been realized through electrical means. Due to the wavelength selection of the resonance ring, this dual channel system is equivalent to containing a pre tunable filter which can be used to increase the sensitivity of the system and is also conducive to the integration of device functions.

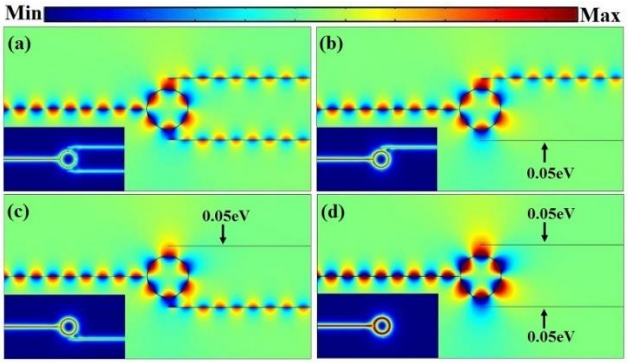

Fig. 6 Magnetic intensity distributions $|H_z|$ with bias on the output arm by a gate voltage: (a) no bias as splitter, lower arm (b) or upper arm (c) biased for digital switch, (d) both bias as off-state. The insets denote the corresponding normalized electric field distributions of graphene SPPs

4. Mach-Zehnder interferometer

Finally, an intriguing fast-tunable ultra-compact Mach-Zehnder interferometer which consists of one input graphene sheet and one output graphene sheet connected through two graphene interference arms and two graphene rings is constructed. The Fermi level on a part of the upper graphene sheet is variable, while the other graphene sheets and two graphene rings are fixed at 0.4 eV, 0.5 eV, respectively. When the resonant light waves are injected from the input graphene sheet, they will be coupled into the two arms and then combine together at the right graphene ring resonator, finally output from the right graphene sheet. The output power is sensitive to the phase difference of SPPs in the two arms, which could be

modulated by changing the propagation constant of graphene SPPs via controlling gate voltage on the graphene. When the Fermi level on one arm becomesE_f', the propagation constant of SPPs changes from β'toβ_{spp}', and hence the effective index fromN_{spp}toN_{spp}'. The phase difference is given by [32]:

$$\Delta\varphi = \arg(t) - \mathrm{Re}\left(\beta_{spp}\right)\cdot L, \qquad (5)$$

where$t = \tau^2 u/(1-\rho^2 u^2)$ is the transmittance of the biased graphene, with $u = \exp(i\beta_{spp}' L)$, $\tau = 2(N_{spp}N_{spp}')^{1/2} / (N_{spp}+N_{spp}')$, and $\rho = (N_{spp}'-N_{spp})/(N_{spp}'+N_{spp})$, ρ and τ are the reflectance and transmittance aroused by the Fermi level variation.

Fig. 7(a) depicts the magnetic intensity distributions $|H_z|$ and normalized electric field distributions of SPPs for the constructive interference when L= 200 nm and the Fermi level on this part of upper graphene arm is 0.4 eV, at which $\Delta\varphi$ = 0. On the contrary, Fig. 7(b) shows the destructive interference case when E_f'= 0.278 eV, at which $\Delta\varphi = \pi$. In Fig. 7(c), we plot the power transmission as a function of the Fermi level. Due to the propagation loss, up to 45% input power can be transmitted through the interferometer. The maxima or minima of transmission indicate whether the SPPs in the arms are in phase or out of phase. We also plot the phase difference of SPPs in the two arms as a function of the Fermi level in Fig. 7(c). Apparently, the maxima are increasing as the Fermi level increases because the Im(β_{spp}) which featuring the propagation loss decreases with the increases of Fermi level. Nevertheless, the Re(N_{spp})increases as the Fermi level decreases leading to smaller spatial oscillation period of SPPs in the upper biased graphene arm as shown in Fig. 7(b). For E_f'= 0.4 eV, 0.214 eV, 0.148 eV, and 0.114 eV, the phase difference $\Delta\varphi \approx 0, 2\pi, 4\pi, 6\pi$. Thus, the transmission reaches its maximum as SPPs are in phase in the arms. For 0.278 eV, 0.174 eV, 0.130 eV, and 0.102 eV, the phase difference $\Delta\varphi \approx \pi, 3\pi, 5\pi, 7\pi$. Thus, the transmission reaches the minimum as SPPs being out phase in the arms. One may notice the $\Delta\varphi$ appear not exactly at the integer times of π. The deviation is due to the reflection of SPPs at the ends of the graphene arms, which is not taken into account in Eq. (5). From 0.35 eV to 0.45 eV, there is a wide band of high transmission with respect to the Fermi level because the phase difference varies slowly around 0 in this region. As already mentioned, the sensitivity of this Mach-Zehnder interferometer can be improved by optimizing the pre tunable filter or the distance between two graphene interference arms and two graphene rings. Thus, we can choose proper coupling distance to balance the transmission power and the sensitivity of system.

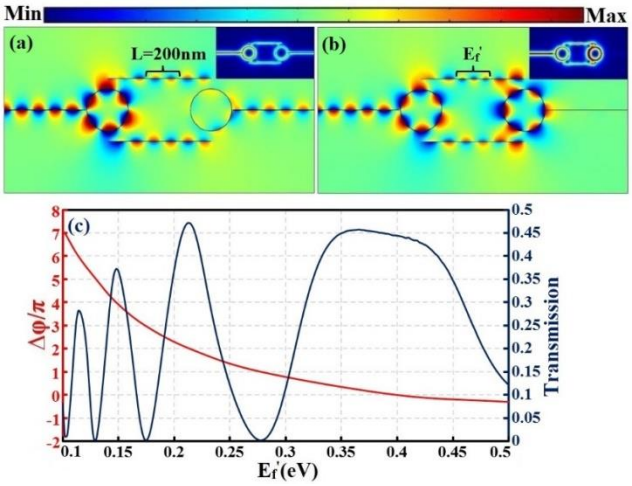

Fig. 7(a) Magnetic intensity distributions $|H_z|$ in a graphene based M-Z interferometer. The two arms have a separation of d = 50 nm to the graphene ring resonators. (b) $|H_z|$ distributions of SPPs in the M-Z interferometer as the upper arm is biased with a gate voltage to form a phase difference of π between the two arms. The insets denote the corresponding normalized electric field distributions of graphene SPPs in the M-Z interferometer. (c) Power transmitted at the output graphene and the phase difference of SPPs in the two arms versus the Fermi level

5. Conclusions

In conclusion, we have numerically demonstrated an ultra-compact Mach-Zehnder interferometer based on a basic graphene plasmonic coupling system composed of graphene sheets and ring resonators for the mid-IR region. Our basic structure can also be used to construct the ultra-compact fast-tunable optical filter, splitter, or 1×2 digital optical switch. The coupling between the graphene sheets and ring resonators has been thoroughly studied. By changing the Fermi level in the graphene rings, the resonant wavelengths can be tuned expediently. Moreover, the quality and sensitivity of the system can be optimized by changing the coupling distance. The FEM results are verified by the resonance theory of the rings. These actively tunable and electrically controlled structures are qualitatively different from traditional SPPs ones which are based on noble metals. We believe that our work could provide new ways toward the realization of nanoscale mid infrared spectral control and graphene plasmonic devices, especially the wavelength filtering, switching and optical modulating elements.

Acknowledgments

This work is supported by the National Natural Science Foundation of China (Grant No. 11504139), the Natural Science Foundation of Jiangsu (Grant No.

BK20140167), and the Key Laboratory Open Fund of Institute of Semiconductors of CAS (Grant No. KLSMS-1604).

References

[1] H. Raether, Springer, Berlin (1998).
[2] T. W. Ebbesen, C. Genet, S. I. Bozhebolnyi, Phys. Today **61**, 44 (2008).
[3] E. Ozbay, Science **311**, 189 (2006).
[4] H. Lu, X. Liu, D. Mao, L. Wang, Y. Gong, Opt. Express **18**, 17922 (2010).
[5] G. Wang, H. Lu, X. Liu, D. Mao, L. Duan, Opt. Express **19**, 3513 (2011).
[6] G. Veronis, S. Fan, Appl. Phys. Lett. **87**, 131102 (2005).
[7] H. Zhao, X. Guang, J. Huang, Physica E **40**, 3025 (2008).
[8] H. Gao, H. Shi, C. Wang, C. Du, X. Luo, Q. Deng, Y. Lv, X. Lin, H. Yao, Opt. Express **13**, 10795 (2005).
[9] S. I. Bozhevolnyi, V. S. Volkov, E. Devaux, J. Y. Laluet, T. W. Ebbesen, Nature **440**, 508 (2006).
[10] K. S. Novoselov, A. K. Geim, S. V. Morozov, D. Jiang, Y. Zhang, S. V. Dubonos, I. V. Grigorieva, A. A. Firsov, Science **306**, 666 (2004).
[11] Z. Q. Li, E. A. Henriksen, Z. Jiang, Z. Hao, M. C. Martin, P. Kim, H. L. Stormer, D. N. Basov, Nat. Phys. **4**, 532 (2008).
[12] D. K. Efetov, P. Kim, Phys. Rev. Lett. **105**, 256805 (2010).
[13] Q. L. Bao, K. P. Loh, ACS Nano **6**, 3677 (2012).
[14] L. Ju, B. Geng, J. Horng, C. Girit, M. Martin, Z. Hao, H. A. Bechtel, X. Liang, A. Zettl, Y. R. Shen, F. Wang, Nat. Nanotechnology **6**, 630 (2011).
[15] B. Wang, X. Zhang, F. J. Garcia-Vidal, X. Yuan, J. Teng, Phys. Rev. Lett. **109**, 073901 (2012).
[16] A. N. Grigorenko, M. Polini, K. S. Novoselov, Graphene plasmonics, Nat. Photonics **6**, 749(2012).
[17] H. S. Chu, C. H. Gan, Appl. Phys. Lett. **102**, 231107 (2013).
[18] Z. Y. Fang, S. Thongrattanasiri, A. Schlather, Z. Liu, L. L. Ma, Y. M. Wang, P. M. Ajayan, P. Nordlander, N. J. Halas, F. J. G. de Abajo, ACS Nano **7**, 2388 (2013).
[19] A. K. Geim, Science **324**, 1530(2009).
[20] S. Thongrattanasiri, F. H. L. Koppens, F. J. G de Abajo, Phys. Rev. Lett. **108**, 047401 (2012).
[21] A. Fallahi, J. Perruisseau-Carrier, Phys. Rev. B **86**, 195408 (2012).
[22] A. Vakil, N. Engheta, Science **332**, 1291 (2011).
[23] G. Zheng, H. Zhang, L. Xu, Y. Liu, Opt. Lett. **41**, 2274 (2016).
[24] J. Lao, J. Tao, Q. J. Wang, X. G. Huang, Laser Photonics Rev. **8**, 569 (2014).
[25] S. Das, A. Salandrino, J. Z. Wu, R. Q. Hui, Opt. Lett. **40**, 1516 (2015).
[26] Q. Qian, Y. Liang, Y. Liang, H. Shao, M. Zhang, T. Xiao, J. Wang, Sensors **16**, 2039 (2016).
[27] H. J. Li, L. L. Wang, H. Zhang, Z. R. Huang, B. Sun, X. Zhai, S. C. Wen, Appl. Phys. Express **7**, 024301 (2014).
[28] S. W. Sheng, K. Li, F. M. Kong, H. W. Zhuang, Opt. Commun. **336**, 189 (2015).
[29] T. J. Echtermeyer, S. Milana, U. Sassi, A. Eiden, M. Wu, E. Lidorikis, A. C. Ferrari, Nano Lett. **16**, 38 (2015).
[30] J. Wang, X. Wang, Z. D. Hu, C. Song, X. Xia, J. Wang, Nanoscale Res. Lett. **12**, 9(2017).
[31] A. Y. Nikitin, F. Guinea, F. J. García-Vidal, L. Martín-Moreno, Phys. Rev. B **84**, 161407 (2011).
[32] Z. R. Huang, L. L. Wang, B. Sun, M. D. He, J. Q. Liu, H. J. Li, X. Zhai, J. Opt. **16**(10):105004, (2014).
[33] P. Y. Chen, A. Alu, ACS Nano **5**, 5855 (2011).
[34] G. W. Hanson, J. Appl. Phys. **104**, 084314 (2008).
[35] W. B. Lu, W. Zhu, H. J. Xu, Z. H. Ni, Z. G. Dong, T. J. Cui, Opt. Express **21**, 10475 (2013).

*Corresponding author: jcwang@jiangnan.edu.cn